PAPER • OPEN ACCESS

Printing thermal performance: an experimental exploration of 3DP polymers for facade applications

View the article online for updates and enhancements.

The Electrochemical Society
Advancing solid state & electrochemical science & technology

DISCOVER how sustainability intersects with electrochemistry & solid state science research

Printing thermal performance: an experimental exploration of 3DP polymers for facade applications

V Piccioni[1], M Leschok[2], G Lydon[13], I Cheibas[4], I Hischier[1], B Dillenburger[2], M Kohler[4], F Gramazio[4], A Schlueter[1]

[1] Architecture and Building Systems, Institute of Technology in Architecture (ITA), ETH Zurich, Switzerland

[2] Digital Building Technologies, Institute of Technology in Architecture (ITA), ETH Zurich, Switzerland

[3] Department of Architecture and Technology, Norwegian University of Science and Technology (NTNU), Trondheim, Norway

[4] Architecture and Digital Fabrication, Institute of Technology in Architecture (ITA), ETH Zurich, Switzerland

E-mail: `piccioni@arch.ethz.ch`

Abstract. The decarbonisation of the building sector requires the development of building components that provide energy efficiency while producing minimal environmental impact. We investigate the potential of polymer 3D printing (3DP) for the fabrication of mono-material translucent facade components, whose properties can be tailored according to climatic conditions and functional requirements. These components bear the potential to reduce energy consumption in buildings and, at the same time, can be fabricated with minimal environmental impact thanks to the recyclability of the feedstock material. In this study, we explore the effect of component geometry on the thermal insulation properties of 3DP objects with bespoke internal structures. Different prototypes are fabricated using a robotic polymer extruder, and their thermal properties are measured following a hot-box test method. The experimental results are then used to calibrate a heat transfer simulation model describing the joint effects of conduction, natural convection and infrared radiation through the components. We show that it is possible to fabricate insulating polymer components providing thermal transmittance ranging from 1.7 to 1 W/m^2K only by changing the internal cavity distribution and size. This proves the possibility of designing 3DP thermally-insulating components for different climatic conditions and requirements. This study provides the first insights into the thermal behaviour of polymer 3DP facades on a large scale. The results suggest that this innovative manufacturing technique is promising for application in facades and encourages further research toward performant and low-embodied energy 3DP building components.

Keywords: polymer 3D-printing, thermal performance, facades, hot-box experiment, FE simulations

1. Introduction

Achieving energy efficiency while minimising environmental impact is a stringent requirement for the decarbonisation of the building sector [1]. In this context, the building facade plays a key role as it greatly impacts the amount of energy needed to provide comfort in buildings.

Moreover, the way facades are constructed significantly contributes to the embodied emission impact of buildings [2]. Therefore, creating high-performance facades is imperative to achieve the Net-zero by 2050 goals.

Advancements in large-scale 3D printing (3DP), in combination with computational design, have shown that it is possible to fabricate building components with embedded performances that can be tuned for their specific application [3; 4]. Thanks to 3DP, designers can not only control the shape of an object but can also define its internal articulation using infill structures to ensure structural integrity during printing and reduce material use [5–7]. Recent studies have focused on the design of infill structures to achieve thermal performance in 3DP wall components, out of earth-based materials [8; 9] and concrete [10–12]. To improve the thermal performance of 3DP concrete elements, concrete mixtures with air inclusions or low conductivity materials can be used [13], and insulating materials can be simultaneously extruded along the concrete layer or fill the infill cavities [14; 15]. However, the inclusion of additional materials compromises the ease of fabrication and assembly, and recyclability.

As an alternative, thermoplastic polymers have also been proposed for the fabrication of facade components, taking advantage of their translucency, light weight and low thermal conductivity. Monomaterial components that integrate thermal insulation and seasonal thermal control have been designed in [16–19]. Most thermal insulation studies investigate millimetre-scale geometrical articulations fabricated using off-the-shelf desktop 3D printers. These infill designs are based on periodic porous structures [20; 21], with limited scalability potential. Recently, large-scale polymer extruders have been used to improve scalability and material output. Those can print polymers with a material output up to 225Kg/h [22], and a generally lower print resolution. To this date, there is little to no research on how the internal articulation of polymer 3DP components influences thermal performance at an architectural scale. This knowledge is required to fabricate thermally insulating 3DP facade elements efficiently.

This study investigates the integration of thermal insulation performance in 3D-printed polymer facades by exploring the interplay of geometry and performance in infill structures. Combining experiments and numerical simulations, we retrieve guidelines for designing thermally insulating 3DP facade elements that provide a low environmental impact yet performant alternative to traditional components.

2. Methods

The following chapter presents the robotic 3DP setup for the creating of bespoke, large-scale prototypes and the design intent for the specimens. After that, we introduce the testing apparatus used for the heat flow experiments and the steady-state method for the thermal characterisation of building components. Finally, we present the experimental procedure, along with the numerical simulation models used for the validation.

2.1. Samples design and 3D printing

To conduct the thermal experiments, we print three different specimens of size 500x500x150mm. These large dimensions are chosen to allow for a 1:1 scale testing scenario. The large area reduces edge effects during the measurements, as sensors can be placed in the centre and far away from the borders/border conditions. The thickness of 150mm results from preliminary studies conducted by the authors. In particular, this thickness is identified to withstand the structural loads considered for application as a 3DP facade.

The specimens are 3D printed using a large-scale polymer extruder mounted on a 6-axis robot (A1). The material chosen for these experiments is PETG, a glycol-modified PET thermoplastic [23]. PETG is a well-known polymer, most often used for medical products or food applications due to its transparency, chemical, and structural resistance [24]. Extrusion-based polymer 3D printing (also referred to as BAAM - Big Area Additive Manufacturing or LSAM - Large Scale
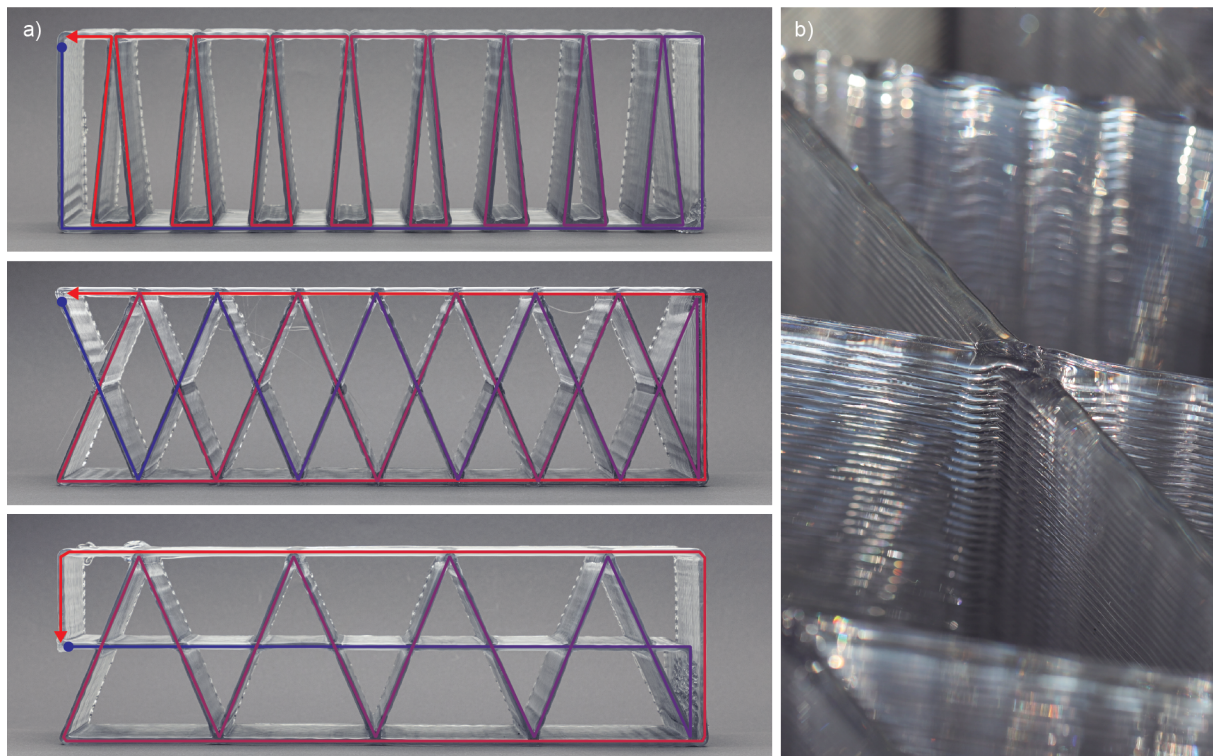
Figure 1. a. Studies on continuous print paths. Different arrangements of infill lines allow for differentiation within the 3DP component. **b.** Close-up of self-intersecting print path, crossing within the same layer forces the material to dwell and form a knot.

Additive Manufacturing) is a process where feedstock material is heated up in an extruder and deposited successively line by line, layer by layer. The extruder used has three different heating zones and a maximum output of 12 kg/h [25]. A 5mm nozzle was used for the fabrication of the specimens. Considering the challenge of creating horizontal surfaces with large-scale polymer 3DP by simple bridging [26], the authors decided to seal the top and bottom surfaces of the specimens by gluing a 3mm polystyrene sheet onto them. The samples are printed with a layer height of 2.5mm and a line thickness of 6mm, resulting in samples between 8.75 and 12.6kg.

The specimens are designed to form a continuous 3D printing path, resulting in a continuous extrusion of material with no start/stop. Intersections can be printed by simple crossing; this way, the material just "dwells" on top of the previous layer, forming a small knot, see Figure 1.b. A continuous print path was chosen due to a lack of a proprietary start/stop mechanism for the printing setup. Compared to continuous print paths, start/stop ones might result in local discontinuities and voids in the printed object. These compromise the parts' air-tightness and therefore have a negative impact on the thermal performance of the object. Figure 1.a shows 3DP studies on continuous infill patterns. The chosen pattern is able to control the dimension of air cavities along the thickness of the element without significantly increasing the amount of material used (Figure 2). It consists of a zig-zag pattern (primary lines) and a separator between the inner and the outer wall of the object (secondary lines). The pattern is kept as simple as possible to ensure good printing quality and ease of study. The distance between the base triangles (primary lines) is kept constant at 125mm, which results, depending on the amount of separator (secondary lines), in a 10 -18% infill percentage. The separator lines divide the air domain within the panel, creating smaller cavities to potentially increase the thermal insulation of the component.
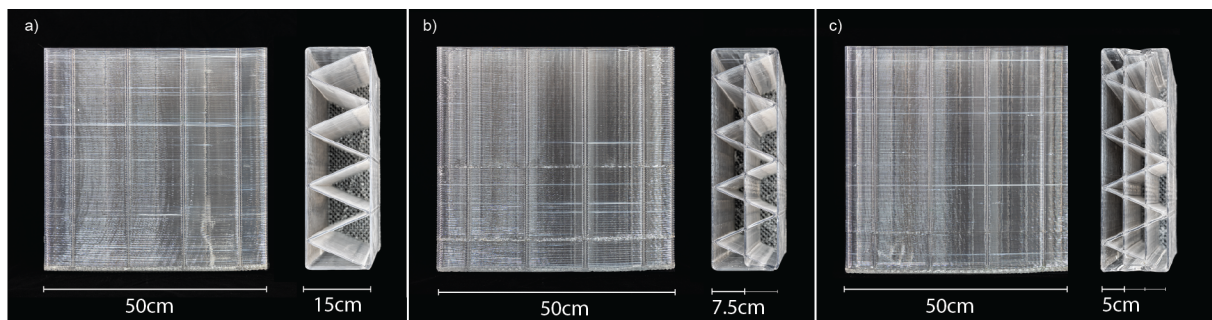
Figure 2. 3D printed specimens for the experimental campaign. **a.** R1, one cavity approx. 15cm. Weight: 8.8kg. **b.** R2, two cavities approx. 7.5cm. Weight: 10.5kg. **c.** R3, three cavities approx. 5cm. Weight: 12.5kg.

2.2. Hot-Box Apparatus

The tests are conducted using a hot-box apparatus, according to the hot-box heat flux meter approach (HB-HFM) [27–29]. The HB-HFM approach is based on the steady-state method for the thermal characterisation of building materials and envelope assemblies [30; 31]. The method measures the heat flux through the component to be studied and the temperature profile across it [32]. The hot-box apparatus comprises a cold chamber kept at a constant low temperature, containing a metering chamber kept at a higher temperature. The specimen to be tested is placed on a mounting ring at the interface between the two chambers. The air temperature inside the metering chamber and in the cold chamber is monitored using platinum resistance thermometers (PT100) and the specimen wall temperatures. The heat fluxes through the specimens are measured using a heat flux transducer.

The experimental setup is in an underground laboratory room enclosed by concrete walls and slabs, ensuring stable temperature conditions and minimal thermal disturbances. The metering chamber consists of a box of dimensions 1 x 1 x 1m approximately (Fig 3. The chamber's walls are made of a thick insulation layer of two XPS panels (2 x 8 cm) and a plywood sheet (2 cm) to ensure minimal heat losses through the structure. The top side of the box consists of a 3.5 cm concrete slab and an outer insulation layer of XPS (8 cm). The concrete slab is the prototype of a thermally active building system (TABS), as described in [33]. It embeds water pipes for cooling and heating through water and takes advantage of the high thermal storage of concrete to dampen temperature peaks. Finally, the front panel comprises a double layer of XPS insulation (22 cm) and accommodates a wooden frame to mount the testing specimen.

A total number of 35 sensors measures the state of the metering chamber (Fig 3.a). Most sensors are placed on the floor and wall surfaces of the metering chamber and on the TABS. Pairs of resistance temperature detectors (RTDs) of type PT100 (Omega Engineering) are placed on each side to measure the specimen's surface temperatures (Fig 3.b,c). Moreover, a heat flux plate of type HFP01 (Hukseflux) is placed in the centre of the specimen's outer surface to measure normal one-dimensional heat flux. Infrared thermography was used to guide the correct placement of thermocouples and heat flux transducer, minimising inaccuracies due to specimen heterogeneity and edge effects (Fig 3.d). The data acquisition is made through a NI cDAQ-9133, and LabView collects and records data with a one-second resolution.

2.3. Experimental Procedure

To better understand the relative effect of air buoyancy on the overall heat transfer, each sample was measured for two different cavity orientations. One measurement is done for the configuration with the cavities running parallel to the ground (along the x-axis, 4.b) and then

rotated by 90 degrees (along the z-axis, 4.a) so the internal cavities allow for air movement from top to bottom. To minimise possible air leakages and to accommodate fabrication tolerances, the specimens are installed in the box by placing a rubber gasket around them. A total of seven RTDs were placed on the specimen: four on the surface exposed to the room and three on the surface exposed to the metering chamber. The sensors are placed in this way to measure the expected extreme surface temperature conditions due to the cavities, either at a full-depth cavity or the connection point of the primary infill lines with the contour of the specimen (4.c).

Experiments start with placing the sample in the metering chamber and activating the pump for water circulation in the TABS at 40 °C. Measurements were performed for a minimum of 72 h to ensure steady-state conditions. For the termination of the test, it was verified that the results obtained at the end of the test do not differ by more than ± 5% compared to the previous 24h [34]. Recorded data show that steady-state conditions are met a few hours after the test initiation due to the elements' low thermal mass; in most cases, the results converge before 24h,
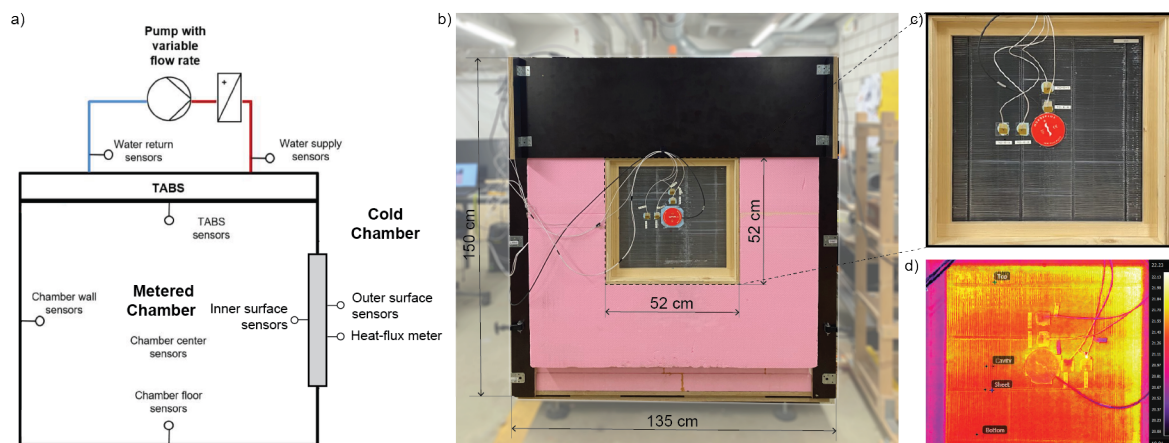

Figure 3. a. Schematics of the hot-box setup. **b.** Front view of the experimental chamber with testing specimen. **c.** Example of RTD and heat-flux sensor placement on testing specimen. **d.** Thermographic images of a tested sample, guiding the sensors placement.
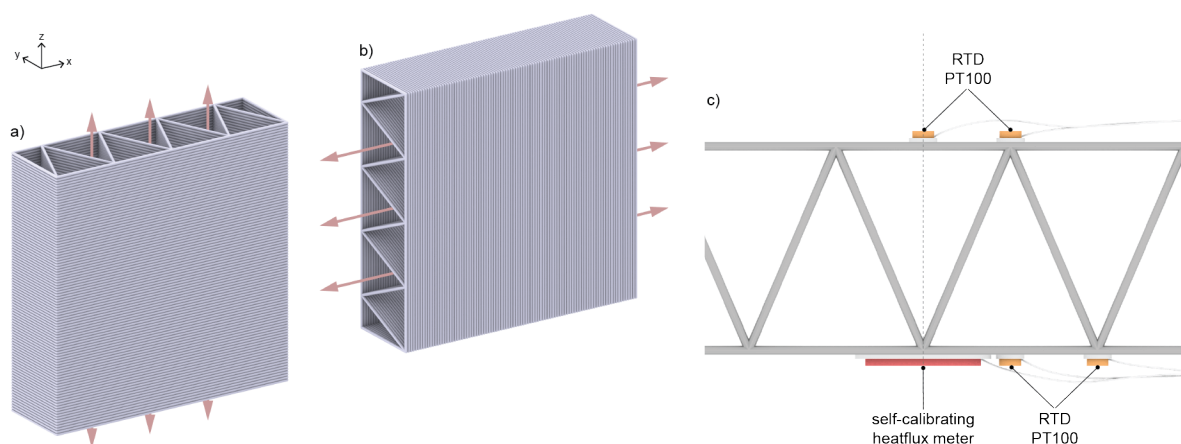

Figure 4. a,b. Schematics showing different testing directions for the 3DP samples. **c.** Schematics of thermal sensor placement, measuring the sample's surface temperatures at the connection of contour and infill and at the middle of an air cavity.

as in Figure 5. This suggests that the duration of the experiments could be greatly reduced.

Data are analysed using the average method [34]. Mean values for heat flow density rate and temperature difference between the two sample's surfaces are obtained by averaging over the last 10h of measurement. As in [35] a value of effective thermal conductivity (λ_{eff}) is derived following the one-dimensional solution of Fourier's law [36]:

$$q = -\lambda_{eff}\frac{dT}{dx} \rightarrow \lambda_{eff} = \frac{qd}{T1 - T2} \, [W/mK] \tag{1}$$

where q is the heat flow throughout the sample per unit area in W/m^2, d is the sample's thickness in m, $T2$ is the temperature of the cold source, $T1$ is the temperature of the hot source, and ΔT is the temperature difference across the sample in K. In order to retrieve standard thermal performance indicator for building elements [34], from the effective thermal conductivity we derive the sample's total thermal resistance (R) and the u-value (U):

$$R_{tot} = R_{si} + \frac{d}{\lambda_{eff}} + R_{se} \, [m^2K/W] \tag{2}$$

$$U = \frac{1}{R_{tot}} \, [W/m^2K] \tag{3}$$

where R_{si} and R_{se} are the resistance of the air boundary layers at the internal and external surface of the component, equal to 8 W/m^{2}K and 25 W/m^{2}K respectively. To reach appropriate confidence, the experimental results of the testing apparatus were benchmarked by performing measurements on a specimen with known thermal characteristics. The experimental procedure was performed on an XPS panel of known thermal properties (λ= 0.035 W/mK). Results from the experiment differ by less than 3% from the nominal properties of the product, which is considered an acceptable accuracy for the experiment.

2.4. Numerical Study

Experimental results were validated against FE simulations simulating the heat transfer through the 3DP samples under experimental conditions. The heat transfer and fluid flow modules of COMSOL Multiphysics® [37] were used for the simulations. Conductive heat transfer happens through the solid thermoplastic domain, with thermal conductivity λ_{petg} equal to 0.2 W/mK [38] and, less significantly, through the fluid domain of the air cavities (λ_{air}= 0.025 W/mK). Convective heat transfer occurs in the cavity and is driven by buoyancy effects originating from air density difference due to the temperature gradient. Radiative heat transfer between the infill walls with emissivity ϵ equal to 0.9, as reported in [39]. Radiation enhances air circulation [40] and strongly depends on the walls surface temperatures. Two heat fluxes are imposed at the two sides of the sample, with a cold temperature (T_{ext}) of 22 °C and a hot temperature (T_{int}) of 35°C, to match the experimental conditions. The boundary conditions are summarised in Figure A2. From the 3D representations, simplified models were created to reduce the computational effort. The models are based on a 2D representation of the samples' geometry. They are modelled using the *heat transfer in solids and fluids* module, coupled with the *surface-to-surface radiation* interface. Two 2D simplifications can be derived from the model by choosing a longitudinal (Figure A2.b) or cross-section (Figure A2.a), section A-A and B-B respectively. The cross section allows the modelling of the triangular-trapezoidal cavities, while the longitudinal section reduces the cavity to two facing walls. For geometries with cavity orientation along the x-axis, air convection is simulated explicitly using the *laminar flow* interface and the Boussinesq approximation [41]. For geometries with cavities along the z-axis, convection is modelled implicitly [42]. The fluid domain is still modelled for conduction, but airflow fields and velocity are not computed. Instead, convection is accounted for by defining
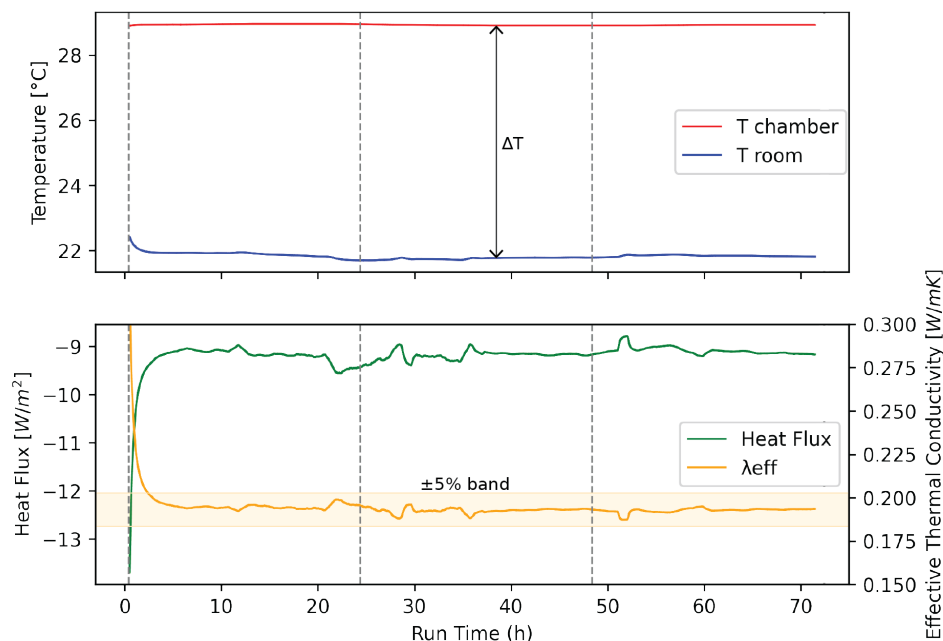
Figure 5. Recorded data during the 72h experiments. **a.** Measured temperatures inside the hot-box (red) and room temperature (blue); **b.** Measured heat flux (green) and calculated effective thermal conductivity (yellow).

an increased thermal conductivity based on an empirical correlation factor that depends on the cavity dimensions and the temperature variation across the cavity. This correlation factor is based on rectangular cavities; therefore, the triangular and trapezoidal cavities are transformed into rectangular air cavities with the same area and aspect ratio, as explained in ISO 10077-2 [43].

3. Results

3.1. Experimental results

The results of the experiments are summarized in Figure 6. An effective thermal conductivity in the range of 0.19 - 0.36 W/mK was observed, corresponding to a U-values from 1 to 1.7 W/m^{2}K. These results confirm the significant effect of geometry on the heat transfer in 3DP components with bespoke cavities. Repetition of the experiments for sample R1 in the two-cavity alignment showed good accordance of results, with an error below 2%. Similarly to porous media, an increase in the number of air cavities inhibits heat transfer and hence positively correlates with thermal insulation [17; 18; 20]. In porous media, however, an increase in air cavity numbers usually results from higher porosity and lower relative density; in our sample, the relative density increases with the number of air cavities due to the additional separating layers. This shows that, for large-scale cavity structures, there is a trade-off between the increase in thermal insulation due to the introduction of air layers and the decrease of insulation due to the enhanced buoyancy-driven effects in wider cavities [44]. Therefore, adding additional cavities in the geometry while keeping the component's width constant correlated to a decrease in effective thermal conductivity, as also reported by [45]. Moreover, it was found that orientation does not affect thermal conductivity significantly for this cavity dimensions. A slightly lower thermal insulation is observed in R1 for the horizontal cavity arrangement, but this effect is not visible in the other samples.

3.2. Numerical results

The 3D FE model allowed observation of the three heat transfer modes through the 3DP component, as shown in Figure A3. The results confirm the presence of a radiative heat exchange between the cavity walls. Moreover, buoyancy-driven air flows develop with the cavities and ultimately affect the thermal stratification in the components.

Results from the 3D and 2D numerical models were compared with the experimental results. Figure 7 shows there is generally good accordance between simulations and experiments, with deviations between 4 - 15%. Furthermore, the trends observed in the experimental study are
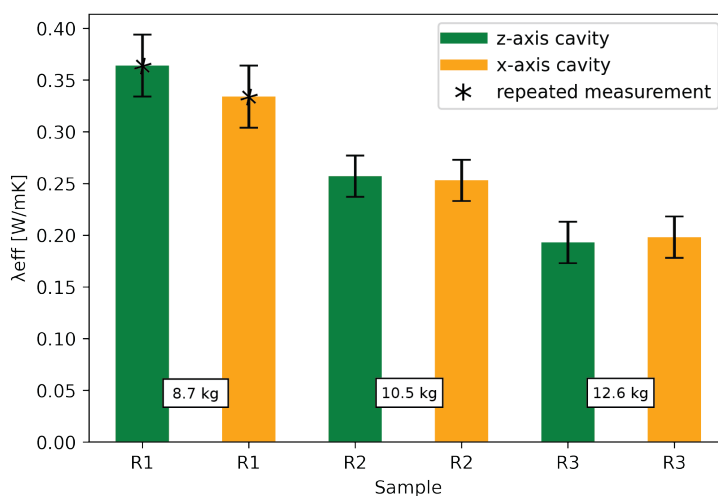

Figure 6. Overview of experimental results: effective thermal conductivity for the six tested samples. Error bars represent the uncertainties of the measurements.
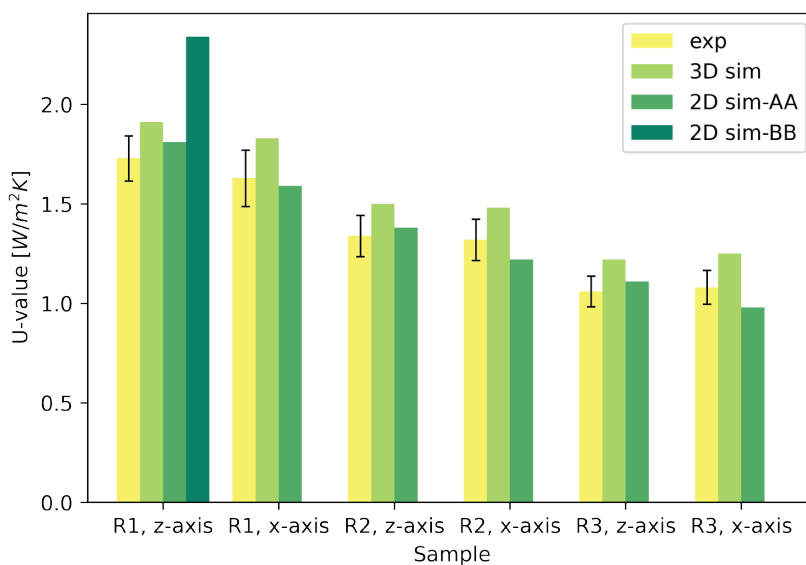

Figure 7. Comparison of results for experiments, 3D and 2D simulations. The error bars represent the measurement uncertainties.

also confirmed in the simulation results. A more significant deviation is found for the 2D model representing section B-B. Compared to the experiments, this model overestimates the thermal transmittance of the component R1 by 35%, assumably due to the impossibility of modelling surface-to-surface radiation between all the cavity walls. The difference between simulated and measured values increases with the number of cavities, which could indicate inaccuracies in the description of the heat transfer mechanisms of multiple cavities in series. Nevertheless, the 2D models based on section A-A can describe the physical behaviour of the system and, thanks to the fast computation time (<1 min), can be effectively used to support the component's design.

4. Conclusions

4.1. Design Guidelines

This study demonstrated the possibility of fabricating facade components through large-scale 3D printing of polymers. It was shown that by managing the cavities' size and arrangement, a reduction in thermal insulation could be achieved by up to 60%. This suggests that tailored 3DP components can be designed according to climate-specific insulation requirements. The combination of experimental and simulation analysis enabled a first understanding of heat transfer mechanisms into 3DP components with internal cavity structures. We observed a trade-off between the increase in thermal insulation due to the air layers and the decrease in insulation due to the enhanced convection effects. Therefore, partitioning the air layers into smaller cavities has proved to decrease thermal transmittance. Moreover, the orientation (x-axis, z-axis) of the cavities does not significantly affect the thermal properties of the components, irrespective of the number of cavities.
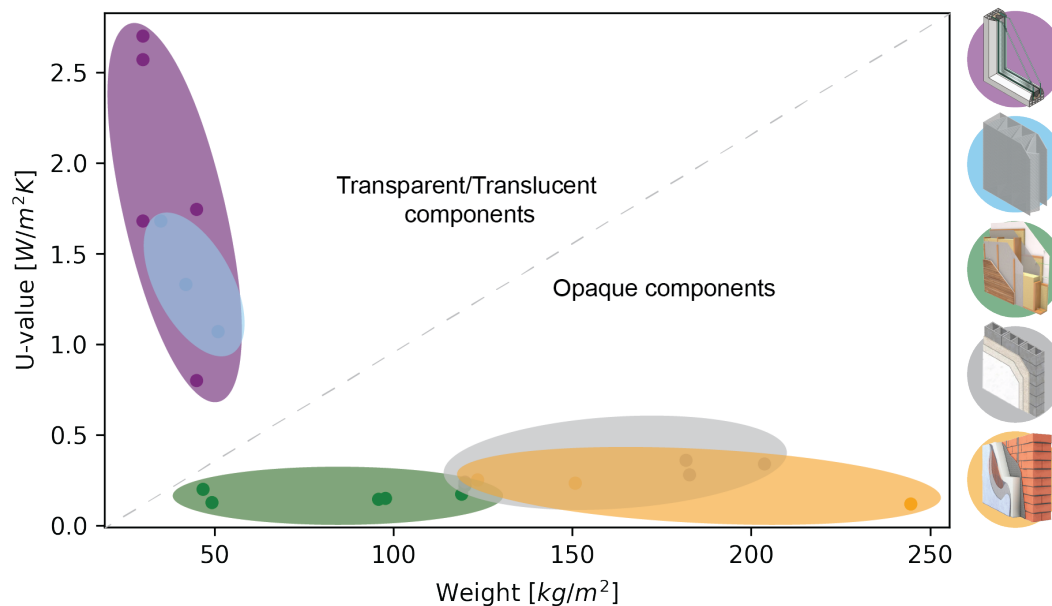

Figure 8. Comparison of thermal performance of 3DP facade and traditional facade components.

4.2. Outlook

The tested prototypes revealed good insulation properties comparable to high-performance triple glazing (Figure 8). Compared with standard facade components, the 3DP components provide

such insulation at a relatively low weight, making them promising for application in buildings (e.g. for retrofits with weight constraints and buildings with lightweight bearing structures). Considerations of the life-cycle environmental impact of 3DP components could further highlight their potential. Compared to standard facade systems, the proposed mono-material 3DP components would be easy to replace and recycle, while the use of recycled polymers would significantly lower their embodied emissions [46].

Building upon this study, the thermal insulation properties of 3DP facades can be further improved by introducing additional cavities within the element thickness. However, creating additional cavities comes with higher weight, printing time and cost, and reduced light transmission, and a trade-off needs to be identified. Using different layer thicknesses for the element, thicker for the outline and thinner for the infill, could help reduce the part's weight while ensuring structural stability. Moreover, polymers with lower thermal conductivity could be investigated such as ABS (λ=0.14-0.21 W/mK) and PP (λ=0.12-0.22 W/mK). Alternatively, the cavities could be filled with a low-conductivity material reducing convective heat transfer. However, this could significantly compromise the component's optical transmission properties and ease of disassembly. Low-emissivity materials/coatings could also be applied to reduce radiative heat transfer in the cavities.

Finally, to fully characterize the performance of translucent 3DP facades, the influence of solar radiation on the heat transfer needs to be investigated, considering the geometrical complexity of the elements. 3D printing creates anisotropic elements with layered resolutions, resulting in angle-dependent, directional transmission of solar radiation [47]. By coupling thermal and optical domains, we can define seasonal/temperature-dependent solar heat gain coefficients (SHGC) and U-values, which would better capture the component behaviour.

Acknowledgements

References
[1] Too J, Ejohwomu O A, Hui F K, Duffield C, Bukoye O T and Edwards D J 2022 *Journal of Cleaner Production* **373** 133858 URL https://doi.org/10.1016/j.jclepro.2022.133858

[2] IEA 2022 Building Envelopes - Analysis and key findings URL https://www.iea.org/reports/building-envelopes

[3] Bischof P, Mata-Falcón J and Kaufmann W 2022 *Cement and Concrete Research* **161** 106948 URL https://doi.org/10.1016/j.cemconres.2022.106948

[4] Jipa M A, Calvo Barentin C J, Lydon G, Rippmann M, Chousou G, Lomaglio M, Schlueter A, Block P and Dillenburger B 2019 3d-printed formwork for integrated funicular concrete slabs *Proceedings of IASS Annual Symposia, IASS 2019 Barcelona Symposium: Advanced Manufacturing and Non-conventional Materials* IASS 2019 (International Association for Shell and Spatial Structures (IASS)) pp 1–8(8) http://hdl.handle.net/20.500.11850/387460

[5] Kontovourkis O and Tryfonos G 2020 *Automation in Construction* **110** 103005 ISSN 0926-5805 URL https://www.sciencedirect.com/science/article/pii/S0926580519300718

[6] Kontovourkis O, Tryfonos G and Georgiou C 2020 *Architectural Science Review* **63** 105–118 ISSN 0003-8628 publisher: Taylor & Francis _eprint: https://doi.org/10.1080/00038628.2019.1620170 URL https://doi.org/10.1080/00038628.2019.1620170

[7] Bos F P, Menna C, Pradena M, Kreiger E, da Silva W R L, Rehman A U, Weger D, Wolfs R J M, Zhang Y, Ferrara L and Mechtcherine V 2022 *Cement and Concrete Research* **156** 106746 ISSN 0008-8846 URL https://www.sciencedirect.com/science/article/pii/S0008884622000370

[8] Dubor A, Cabay E and Chronis A 2018 Energy Efficient Design for 3D Printed Earth Architecture *Humanizing Digital Reality: Design Modelling Symposium Paris 2017* ed De Rycke K, Gengnagel C, Baverel O, Burry J, Mueller C, Nguyen M M, Rahm P and Thomsen M R (Singapore: Springer) pp 383–393 ISBN 978-981-10-6611-5 URL https://doi.org/10.1007/978-981-10-6611-5_33

[9]   Gomaa M, Carfrae J, Goodhew S, Jabi W and Veliz Reyes A 2019 *Architectural Science Review* **62** 230–237
      ISSN 0003-8628 publisher: Taylor & Francis _eprint: https://doi.org/10.1080/00038628.2019.1606776 URL
      `https://doi.org/10.1080/00038628.2019.1606776`

[10] Dielemans G, Briels D, Jaugstetter F, Henke K and Dörfler K 2021 *Journal of Facade Design and Engineering*
      59–72 Pages artwork Size: 59-72 Pages Publisher: Journal of Facade Design and Engineering URL
      `https://journals.open.tudelft.nl/jfde/article/view/5418`

[11] Marais H, Christen H, Cho S, De Villiers W and Van Zijl G 2021 *Journal of Building Engineering* **41** 102431
      ISSN 2352-7102 URL `https://www.sciencedirect.com/science/article/pii/S2352710221002886`

[12] Sun J, Xiao J, Li Z and Feng X 2021 *Energy and Buildings* **241** 110965 ISSN 0378-7788 URL `https:`
      `//www.sciencedirect.com/science/article/pii/S0378778821002498`

[13] Briels D, Kollmannsberger S, Leithner F, Matthäus C, Nouman A S, Oztoprak O and Rank E 2022
      Buildings **12** 1023 ISSN 2075-5309 number: 7 Publisher: Multidisciplinary Digital Publishing Institute
      URL `https://www.mdpi.com/2075-5309/12/7/1023`

[14] Pessoa S, Guimarães A S, Lucas S S and Simões N 2021 *Renewable and Sustainable Energy Reviews* **141**
      110794 ISSN 1364-0321 URL `https://www.sciencedirect.com/science/article/pii/S1364032121000897`

[15] Furet B, Poullain P and Garnier S 2019 *Additive Manufacturing* **28** 58–64 ISSN 2214-8604 URL `https:`
      `//www.sciencedirect.com/science/article/pii/S2214860418307103`

[16] Tenpierik M, Turrin M, Wattez Y, Cosmatu T and Tsafou S 2018 *Spool. Journal of Architecture and the
      Built Environment* **5** ISSN 2215-0897

[17] Sarakinioti M V, Turrin M, Konstantinou T, Tenpierik M and Knaack U 2018 *Materials Today
      Communications* **15** 275–279 ISSN 2352-4928 URL `https://www.sciencedirect.com/science/article/`
      `pii/S2352492817301502`

[18] Piccioni V, Turrin M and Tenpierik M 2020 A Performance-Driven Approach for the Design of Cellular
      Geometries with Low Thermal Conductivity for Application in 3D-Printed Façade Components *Proceedings
      of the Symposium on Simulation for Architecture and Urban Design (SimAUD 2020) Society for Computer
      Simulation International (SCS).* ed Chronis A , Wurzer G, Lorenz W E L, Herr C M, Pont U, Cupkova D
      and Wainer G p 327:344

[19] Mungenast M B 2019 *3D-Printed Future Facade* Dissertation Technische Universität München München

[20] Alqahtani S, Ali H M, Farukh F, Silberschmidt V V and Kandan K 2021 *Journal of Building Engineering* **39**
      102243 ISSN 2352-7102 URL `https://www.sciencedirect.com/science/article/pii/S2352710221000991`

[21] Grabowska B and Kasperski J 2020 *Materials* **13** 4400 ISSN 1996-1944 URL `https://www.ncbi.nlm.nih.`
      `gov/pmc/articles/PMC7579224/`

[22] Marrett D Lsam - large scale additive manufacturing URL `https://www.thermwood.com/lsam_home.htm`

[23] Sepahi M T, Abusalma H, Jovanovic V and Eisazadeh H 2021 *Journal of Materials Engineering
      and Performance* **30** 6851–6861 ISSN 1059-9495, 1544-1024 URL `https://link.springer.com/10.1007/`
      `s11665-021-06032-4`

[24] Petrov P, Agzamova D, Pustovalov V, Zhikhareva E, Saprykin B, Chmutin I and Shmakova N 2021
      ESAFORM 2021 URL `https://popups.uliege.be/esaform21/index.php?id=3763`

[25] CEAD L S A M E25 E25 Printing head URL `https://ceadgroup.com/solutions/technology-components/`
      `e25/`

[26] Eyercioglu O, Aladag M, Aksoy A and Gov K 2019 DETERMINATION OF THE MAXIMUM BRIDGING
      DISTANCE IN LARGE SCALE ADDITIVE MANUFACTURING *4th International Congress on3D Printing
      (Additive Manufacturing) Technologies and Digital Industry* (Antalya) p 10

[27] Amaral C, Vicente R, Ferreira V and Silva T 2017 *Energy and Buildings* **153** 392–402 ISSN 03787788 URL
      `https://linkinghub.elsevier.com/retrieve/pii/S0378778817309453`

[28] Meng X, Gao Y, Wang Y, Yan B, Zhang W and Long E 2015 *Applied Thermal Engineering* **83** 48–56 ISSN
      13594311 URL `https://linkinghub.elsevier.com/retrieve/pii/S1359431115002252`

[29] Buratti C, Belloni E, Lunghi L and Barbanera M 2016 *International Journal of Thermophysics* **37** 47 ISSN
      0195-928X, 1572-9567 URL `http://link.springer.com/10.1007/s10765-016-2052-2`

[30] C16 Committee ASTM International 2019 Practice for Calculating Thermal Transmission Properties Under
      Steady-State Conditions Tech. rep. ASTM International URL `http://www.astm.org/cgi-bin/resolver.`
      `cgi?C1045-07`

[31] C16 Committee ASTM International 2019 Test Method for Thermal Performance of Building Materials and Envelope Assemblies by Means of a Hot Box Apparatus Tech. rep. ASTM International URL `http://www.astm.org/cgi-bin/resolver.cgi?C1363-19`

[32] Soares N, Martins C, Gonçalves M, Santos P, da Silva L S and Costa J J 2019 *Energy and Buildings* **182** 88–110 ISSN 03787788 URL `https://linkinghub.elsevier.com/retrieve/pii/S037877881831836X`

[33] Lydon G, Caranovic S, Hischier I and Schlueter A 2019 *Energy and Buildings* **202** 109298 ISSN 03787788 URL `https://linkinghub.elsevier.com/retrieve/pii/S0378778819305201`

[34] ISO/TC 163/SC 1 Test and measurement methods 2014 Thermal insulation — building elements — in-situ measurement of thermal resistance and thermal transmittance — part 1: Heat flow meter method Standard International Organization for Standardization Geneva, CH

[35] Sánchez-Calderón I, Merillas B, Bernardo V and Rodríguez-Pérez M 022 *Journal of Thermal Analysis and Calorimetry* **147** 12523–12533 ISSN 1588-2926 URL `https://doi.org/10.1007/s10973-022-11457-7`

[36] Çengel Y A 2003 *Heat Transfer: A Practical Approach* (McGraw-Hill) ISBN 978-0-07-245893-0 google-Books-ID: nrbfpSZTwskC

[37] Apache Software Foundation Comsol multiphysics® v. 5.6 URL `https://www.comsol.com/`

[38] MatWeb Database 2021 Overview of materials for petg copolyester data is a summary of similar materials in the MatWeb database for the category PETG Copolyester. `https://www.matweb.com/search/datasheet_print.aspx?matguid=4de1c85bb946406a86c52b688e3810d0`

[39] Badarinath R and Prabhu V 2022 *Materials* **15** 618 URL `https://doi.org/10.3390/ma15020618`

[40] Mezrhab A, Bouali H, Amaoui H and Bouzidi M 2006 *Applied Energy* **83** 1004–1023 URL `https://doi.org/10.1016/j.apenergy.2005.09.006`

[41] Kleinstreuer C 2005 *Engineering Fluid Dynamics: An interdisciplinary systems approach* (Cambridge University Press) chap 2.2.2 Derivation of a Generalised Transport Equation, pp 53–56

[42] Frei W 2017 Modeling natural and forced convection in comsol multiphysics® URL `https://www.comsol.com/blogs/modeling-natural-and-forced-convection-in-comsol-multiphysics/`

[43] ISO/TC 163/SC 2 Calculation methods 2017 Thermal performance of windows, doors and shutters — calculation of thermal transmittance — part 2: Numerical method for frames Standard International Organization for Standardization Geneva, CH

[44] Zhu J and He G 2019 *Science and Technology for the Built Environment* **25** 1143–1151 URL `https://doi.org/10.1080/23744731.2019.1624447`

[45] Suntharalingam T, Gatheeshgar P, Upasiri I, Poologanathan K, Nagaratnam B, Rajanayagam H and Navaratnam S 2021 *Sustainability* **13** 2314 URL `https://doi.org/10.3390/su13042314`

[46] Zhou S 2021 *An Environmental Perspective on 3DPrinted Façade with Plastics* Master's thesis ETH Zürich Switzerland

[47] Piccioni V, Leschok M, Grobe L O, Wasilewski S, Hischier I and Schlüter A in press 2023 *Advanced Materials Technologies* URL `http://doi.org/10.1002/admt.202201200`

Appendix A.

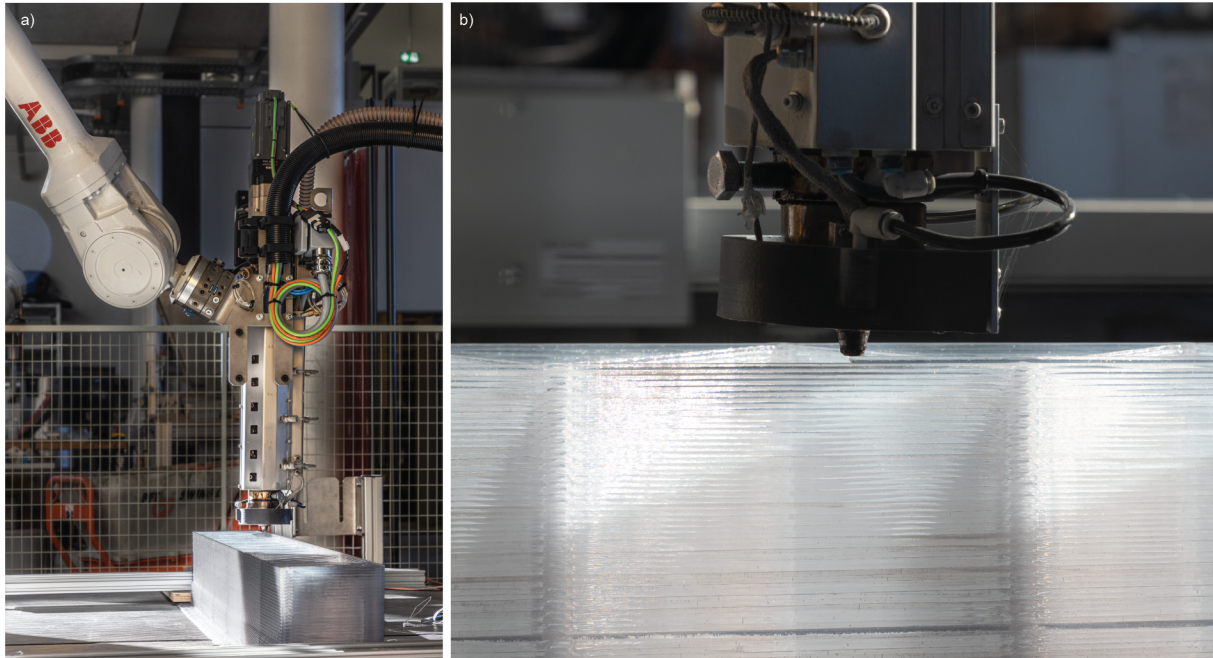**Figure A1. a.** Robotic 3D printing setup, comprising a CEAD E25 extruder mounted on an ABB IRB4600. **b.** Close-up of the polymer printing process: PETG printed with 2.5mm layer height and 6mm layer width.
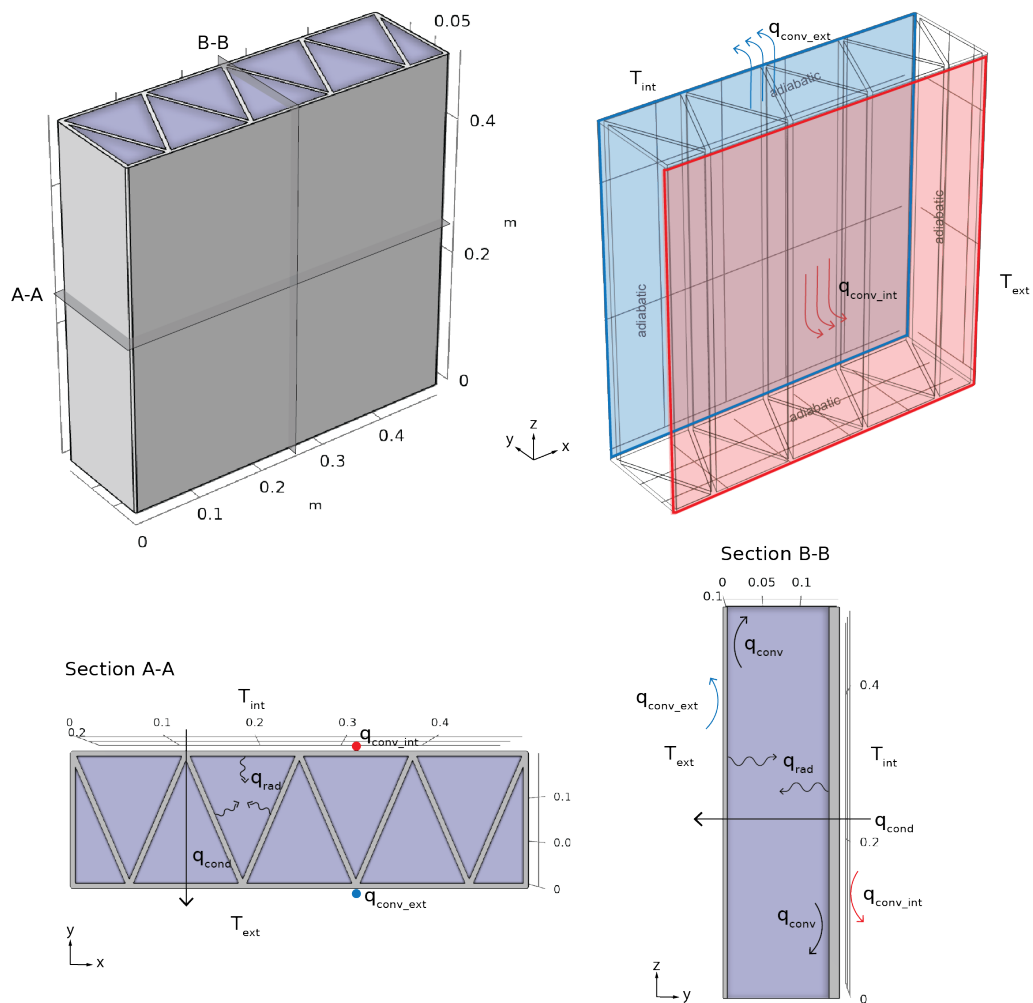
Figure A2. Boundary conditions for the numerical models. **a.** 3D model of sample R1 for the FE simulation. From this, 2D representation are derived based on the cross-section **b.** and the longitudinal section
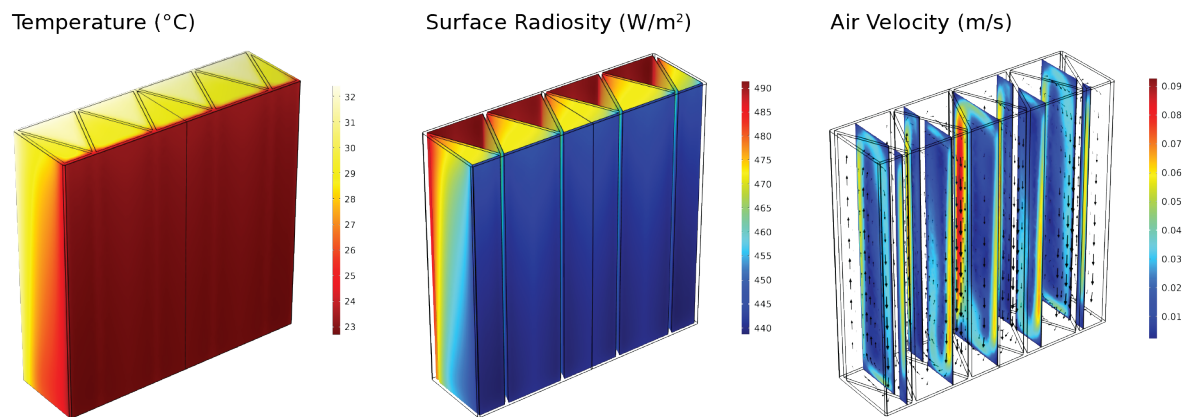
Figure A3. FE simulation results for sample R1. The joint effects of radiative, convective and conductive heat transfer influence the thermal stratification in the sample.